

Modeling and assessing the potential of the Boqueirão channel for tidal exploration[☆]

Diego L.S. Cosme^{a,1}, Rafael B. Veras^{a,1}, Ramiro G.R. Camacho^{b,1}, Osvaldo R. Saavedra^{a,*,1}, Audálio Torres^{c,1}, Mauro M. Andrade^{d,1}

^a Electrical Energy Institute, Federal University of Maranhão, Brazil

^b Federal University of Itajuba, Brazil

^c Federal University of Maranhão, Brazil

^d University of Vale do Itajaí, Brazil

ARTICLE INFO

Keywords:

Tidal energy
Renewable energy
Ocean energy
Tidal streams

ABSTRACT

Exploring the energy potential of the oceans is a promising alternative to produce clean energy with a reduced environmental impact. Brazil has a significant tidal potential, particularly in the coastal region of the north, which covers the states of Amapá, Pará and Maranhão. The Boqueirão Channel, located in São Marcos Bay in Maranhão, is recognized for its wide tidal variability and strong tidal currents, which shows it has a significant tidal potential. This article examines the energetic characterization of this estuary in terms of tidal currents. Based on measurements taken in situ using an Acoustic Doppler Current Profiler and a Conductivity, Temperature and Depth sensor, the area is modeled in Delft3D software, with velocity results adjusted and validated to allow accurate representation of tidal currents. The theoretical potential of an area of 1.5 km², considering a hydrokinetic turbine with diffuser, was estimated at 85.75 GWh. The results obtained are compared with those in the literature. Taking into account the available area and the physical constraints of the channel, it is possible to estimate a Levelized Cost of Energy - LCOE of 0.185 \$kWh⁻¹ for the projected hydrokinetic farm.

1. Introduction

Renewable energy sources are becoming increasingly important worldwide as a result of the effects of global warming. The global energy mix is in a phase of change, and increasing its share of non-polluting and renewable energy resources. According to the BP annual energy report for 2020 [1], there was a 1.3% reduction in electricity generated from burning coal, which led it to having a 35.1% share in the world energy matrix. Another positive statistic in the same year was the record amount of renewable sources that reached 11.7%.

In light of this, it is worth highlighting the oceanic sources. The main forms of oceanic generation are as follows: tidal currents, tidal barrage, waves, OTEC (Ocean Thermal Energy Conversion) and salinity gradient [2].

The total electrical power generated from marine sources is still at an early stage and reached 534.7 MW in 2020, mostly from tidal barrage [2]. This form of energy extraction is the most consolidated, with La Rance Tidal Power Station being the pioneer plant that was

installed in France in 1966. Since that time, there have been significant technological developments in the assembly and manufacture of materials, cables and communications infrastructure services that have had a positive impact on all forms of oceanic energy [3].

There are a few places in the world where the speed of tidal currents is very high (in the order of 3 or 4 ms⁻¹). However, currents of lower intensity, but still with significant potential for extractable energy, are more often found in estuaries and rivers around the world. For example, approximately 70 % of the navigable Channels of the coast of China, have average speeds below 1.5 ms⁻¹ [4]. The south, west and east coasts of the UK are also included in the category of average current speeds of less than 2 ms⁻¹. Portugal is facing the challenge of harnessing tidal energy from the Rio Formosa Channel, where the speed of currents does not exceed 1.4 ms⁻¹.

In [5], there is an investigation of the tidal and river in-stream energy in the Shannon Estuary of Ireland. The authors used a high-resolution numerical modeling and conducted a spatial analysis. The

[☆] We would like to thank to CNPQ, Brazil and FAPEMA, Brazil for its financial support.

* Corresponding author.

E-mail address: o.saavedra@ieee.org (O.R. Saavedra).

¹ All co-authors had the same degree of contribution to the article.

maximum current velocities obtained registered peaks of up to 2.3 ms^{-1} during the ebb tide. The area with the highest power density corresponded to the strongest flows, with 2 kWm^{-2} followed by the other hotspots, with 1.2 kWm^{-2} to 0.5 kWm^{-2} .

In [6], the authors describe the development and validation of a high resolution three-dimensional tidal hydrodynamic model of the Salsish Sea, and conduct tidal stream resource characterization at hotspots based on model outputs. A total of 16 representative sites were selected for potential tidal energy development on the basis of velocity magnitude and channel depth criteria. From the findings of these studies, the authors concluded that both current magnitude and kinetic energy must be calculated when selecting appropriate tidal hotspots for deploying tidal energy plants.

In South-East Asia, medium current intensities also predominate, which are less than 2 ms^{-1} . In the Philippines and Malaysia, flows were limited to 1.4 and 1.2 ms^{-1} , respectively. Mexico has flow conditions similar to those found in Brazil - around 1.5 to 2 ms^{-1} [7]. The North and North-East regions of Brazil are among the main locations considered to be feasible for the exploitation of energy from tidal currents [8].

In addition to the growing number of works concerned with sites that have moderate tidal currents, there are several that address the question of which turbines are most suitable for these conditions (i.e., lower cut-in speed), as well as for small and medium-sized projects that are highlighted in the current literature [9]. For example, in [10], the authors investigate the possibility of installing a hydrokinetic farm in the port of Ribadeo (Spain) which consists of 25 turbines with diameter of 4.5 m and cut-in speed of 0.7 ms^{-1} .

There are many sites with good tidal energy indicators that have heavy shipping traffic, limited depth and an irregular marine topography. A non-conflicting operation is to use smaller turbines when forming a hydrokinetic farm. In view of these restrictions, the farm must be optimized, both in its topology and in the turbine model, since the degree of efficiency obtained from an unconfined flow is restricted by the Betz limit [11].

In [12] the concept of a hydrokinetic diffuser-augmented turbine (HDAT) is discussed. The diffuser brings about a reduction in the tip vortices of the propellers and makes the flow passing through the turbine more laminar [13].

From a hydrodynamic standpoint, after the water passes through the turbine, a spiral flow region is created, called wake turbulence [13]. The extension of this wake has a direct impact on the spacing of the turbines in a hydrokinetic farm [14].

This article examines the modeling and energetic characterization² of tidal currents³ in the Boqueirão Channel. Following this, a hydrokinetic park is designed, as a case study which takes into account the semi-enclosed morphology of the estuary. This includes HDATs with an optimized topology, and takes note of the wake effect. The main research contributions made by this article are:

- A demonstration of the potential tidal energy of the estuary; and
- A feasibility assessment of the use of HDATs in a tidal wave farm.

² In this work, the term ‘characterization’ refers to a preliminary study that serves as a basis for resource assessment. However, for a comprehensive evaluation, more measurement time is required, as established by the standard IEC TS 62600-201:2015. This standard establishes a system for analyzing, through estimation or direct measurement, the theoretical energy potential of tidal currents in oceanic areas, including estuaries (up to the limit of tidal influence), which may be suitable for the installation of Tidal Energy Converters arrays.

³ In this study, the word ‘current’ is differentiated from ‘tidal current’ since the measurement based on the ADCP method also includes currents caused by the wind and flow of the local river, while data from the modeling only includes tidal currents.

The article is structured as follows: Section 2 characterizes the Boqueirão Channel; Section 3 describes the data obtained from the measurement campaigns; Section 4 illustrates the DELFT3D modeling; Section 5 estimates the potential of tidal energy production; Section 6 suggests a dimensioning of the hydrokinetic farm to be installed; Section 7 makes a cost estimate of the project, and finally Section 8 summarizes the conclusions of the article.

2. Characterization of the target area

São Marcos Bay is located in the State of Maranhão, in northern Brazil (Fig. 1.a). This area has been the subject of some researches including hydrodynamic modeling and identifying energy hotspots [15–17]. The bay is supplied with fresh water discharges from the rivers Pericumã, Mearim and Itapecuru, which together form the São Marcos estuarine complex. The site has a dry and wet season which are well-defined. It has a large tidal range and strong currents, particularly in the Boqueirão Channel. This Channel has a width of around 900 m and a depth ranging from 20 to 30 m [16,18]. It is located between São Luís Island (Fig. 1.b) and Medo Island (Fig. 1.c).

The tidal ranges in the Channel have MHWS (Mean High Water Springs) of 6.02 m and MHWN (Mean High Water Neaps) of 4.87 m [19] with a water regime characterized by semi-diurnal tides, with two high tides and two low tides per lunar day, occurring at proportional intervals of 6 h [20–22].

3. Measurement campaigns

Two in loco measurement (mooring) campaigns were carried out for a more detailed analysis of the energy potential of the Boqueirão Channel. The first, from November 9 to 10, 2021 and the second, from February 2 to 3, 2022. The location coordinates are 2° 31'44.8" S (latitude) and 44° 21'42.8" W (longitude). In Fig. 2, this location is illustrated, with the aid of the “Measurements” marker.

The first campaign was carried out in the neap⁴ tide, when the moon was in the crescent phase [23]. It started at 8:30 on 11-09-2021 and ended at 9:36 on 11-10-2021. The period covered two high tides and two low tides. The high tides were at 09:35 (5 m) and 22:00 (5.2 m). The low tides at 16:00 (0.8 m) and 04:50 (0.7 m).

The second campaign was carried out during the spring tide, when the moon was in the new phase [23]. It started at 7:28 on 02-02-2022 and ended at 7:30 on 03-02-2022. As in the case of the previous mooring, this campaign also covered two low tides and two high tides. The high tides occurred at 7:30 (5.7 m) and 19:40 (6.2 m) respectively. The low tides occurred at 14:20 (0.4 m) and 02:40 (0.0 m) respectively.

During the campaigns, a 1 MHz Bottom-Tracking Sontek[®] ADCP, coupled with a Garmin[®] GPS (Global Positioning System), was used. It was configured to continuously record a profile (averaging interval) every 60 s in 1-meter-sized cells, with a blank distance of 0.5 m and a draft of 0.2 m. The magnetic declination value of -20.4° was defined into the configuration and taken into account during the measurements. Additionally, during flood and ebb tides, a significant difference in the equipment's equilibrium position (heading change) was observed, but the ADCP accounts for this effect due to its internal compass.

Before starting the first measurement, still on the boat itself, the calibration of the ADCP's inclination sensors and internal compass was performed, following the equipment manufacturer's specifications. This way, errors caused by external interference are eliminated, and the generated data offers higher quality.

⁴ The new moon occurred on 11–04. The tidal peak in the region usually occurs two days after the new moon. In this specific case, the tidal peak was 6.5 m on 11–06. The measurement campaign actually took place during a transitional period near the first quarter lunar phase, so we refer to it as the neap measurement campaign.

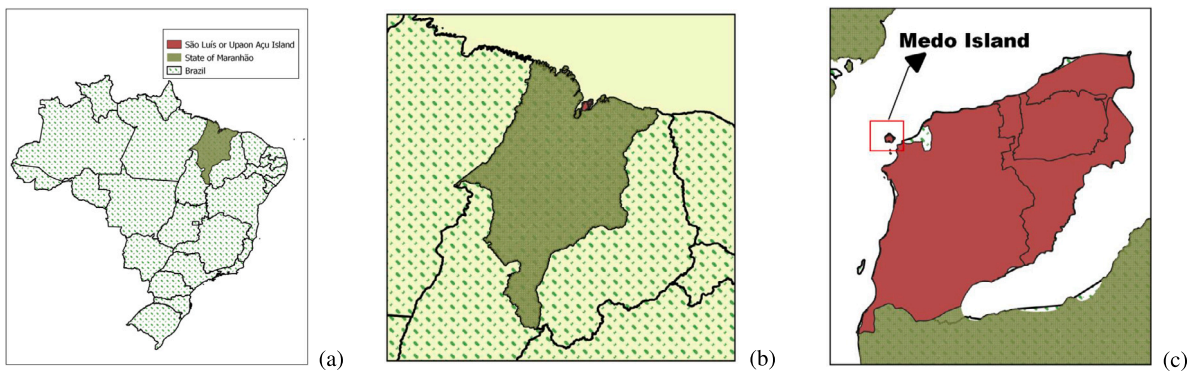


Fig. 1. Location of the target area. Map of Brazil highlighting the State of Maranhão 1.a; Map of the State of Maranhão 1.b; Islands of São Luís and Medo 1.c.

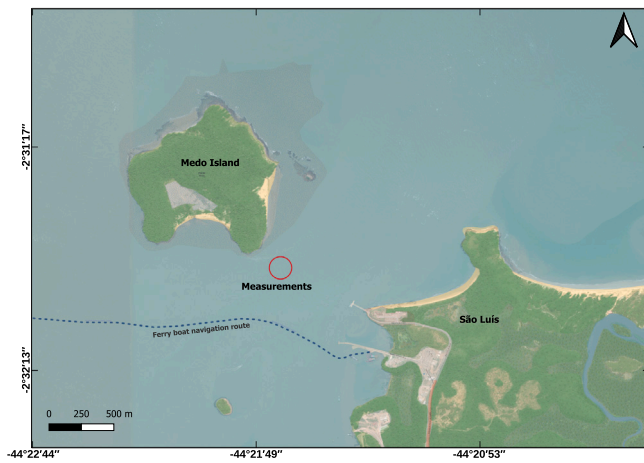


Fig. 2. Mooring place for data collection. Medo and São Luís islands are highlighted.

At the same time, measurements were made of the vertical profiles of temperature, salinity and turbidity every hour by means of a multiparameter sonde (CTD, Conductivity, Temperature and Depth), YSI brand, EXO model 1. Fig. 3.a illustrates the CTD with a counterweight. Fig. 3.b shows the conductivity, temperature and pressure sensors. Fig. 3.c illustrates the ADCP before installation, and Fig. 3.d shows the GPS-ADCP system installed for the measurements.

Fig. 4 displays a Hovmöller diagram, which represents 2D water temperature and salinity distributions in the Boqueirão Channel as a function of time. It was observed that there was no significant stratification in the profile, which shows uniform values of salinity and temperature. The average temperature observed was 29.1 °C, with an approximate variation of 0.24 °C. The salinity values ranged from 31.8 to 33.5 psu, and showed an increase with flood currents covered between low and high tides.

Fig. 5.a illustrates the magnitude and direction of the current obtained during the neap tide, while Fig. 5.b displays data from the spring tide. Since Mooring 1 took place at neap tide, the magnitudes of the velocities were between 1.5 and 2 ms⁻¹, both in flood and ebb.

Mooring 2 occurred during a spring tide with a predominance of speeds greater than 2 ms⁻¹ in the flood. In the ebb tide the predominance of magnitudes was between 1.5 and 2 ms⁻¹. It is worth noting that the directions of flood and ebb currents are almost diametrically opposite.

In Fig. 6⁵ the speed of currents obtained in the neap and spring tide are displayed for the depths (referred to as layer in the graph) of

⁵ When plotting this graph, only the magnitude of the velocity vector is considered and whether the current is ebb or flood. It is assumed that if

Table 1

Total time duration of each velocity amplitude in both spring and neap tide measurement campaigns.

Speed	Total duration time (%)	
	Neap tide	Spring tide
0.5	89.6	91.1
1	73.2	78.7
1.5	47.4	61.5
2	2.3	28.3
2.5	0	0.2

1, 5, 10, 15 and 19 m. Note that closer to the bed, the velocities are significantly lower, owing to the seabed friction. The maximum current speed observed was 2.31 ms⁻¹ at 13:05. Fig. 6.b shows the magnitudes obtained during the spring tide. The maximum magnitude of speed that was recorded was 2.58 ms⁻¹, at a depth of 5 m at 17:30.

Fig. 7 shows the average current speed profile for different levels of Channel depth for both campaigns. The red curve represents the neap mooring and the blue curve represents the spring mooring. The negative average values refer to the intensities measured in the flood tide and the positive ones in the ebb tide.

During both periods, the current speeds were relatively homogeneous at the depth levels, in particular for more intermediate distances, for example, up to 16 m. Even in the case of the greatest depths, the standard deviations of the average intensities in the neap and spring moorings were 13% and 14%, respectively. This homogeneous velocity in the vertical profile is a good characteristic of this site, especially with regard to the problem of mechanical stress in hydrokinetic turbines.

Table 1 summarizes the amount of time when currents were higher than the velocities of 0.5, 1, 1.5, 2 and 2.5 ms⁻¹, respectively, for the neap and spring tide campaigns. This table also considers depths up to 16 m. For example 48% of the time we have velocity above 1.5 ms⁻¹ for the case of quadrature and 62% for spring tide.

The indicators described in this section are in accordance with those of previous studies that show a good hydrokinetic energy potential in the region [16,24].

4. Hydrodynamic modeling of the Boqueirão channel

The open-source platform Delft3D-FLOW was used for hydrodynamic modeling. The choice of curvilinear grids is advantageous as it provides high resolution in the area of interest and low resolution in other areas, reducing computational effort. Additionally, these

the direction angles of the current velocity vector are greater than 180°, the velocity magnitude will be negative and represent the flow of the flood current. If it is less than, or equal to 180°, its magnitude will be positive and will represent the flow of the ebb current.

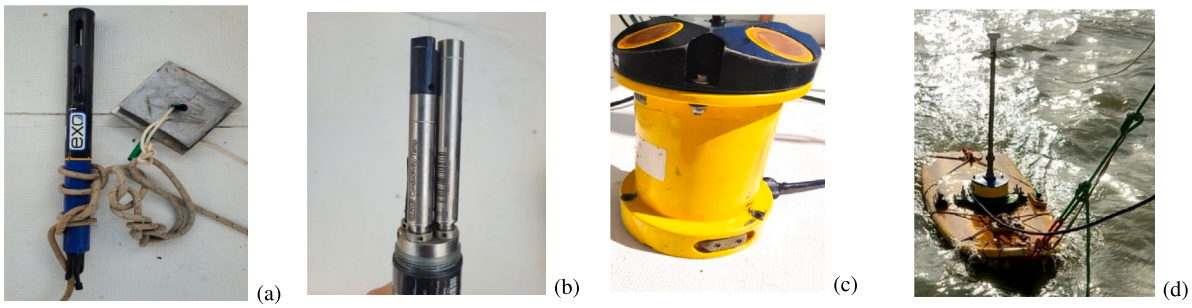


Fig. 3. The CTD and ADCP used during the campaigns. (a) CTD with counterweight; (b) Conductivity, temperature and depth sensors; (c) ADCP sensor; (d) Sensor with GPS attached and installed on a board.

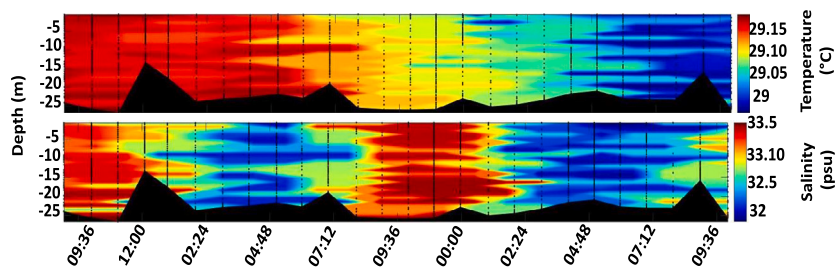


Fig. 4. Hovmöller diagram of the Boqueirão Channel during neap tide.

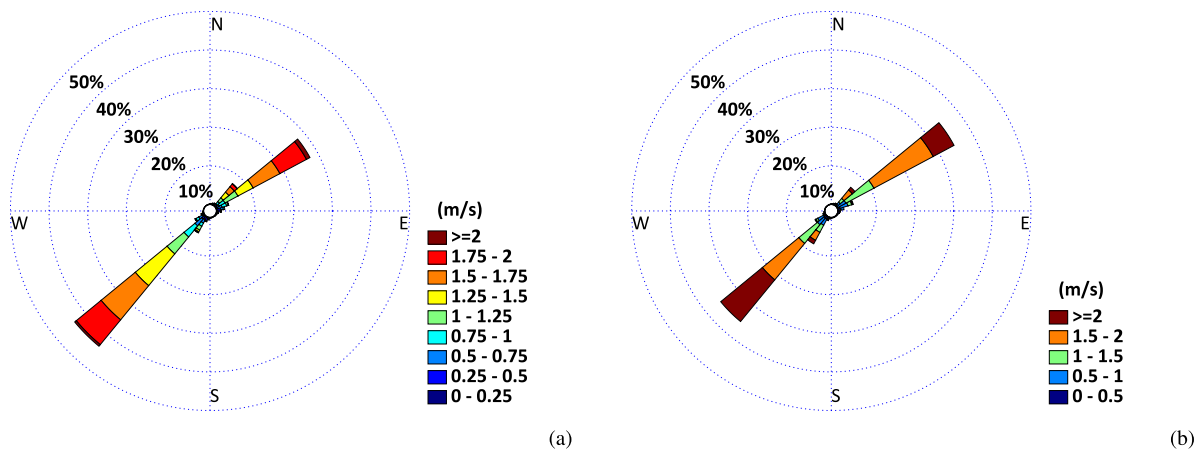


Fig. 5. Direction of the current vector measured in the neap (a); and spring tide (b).

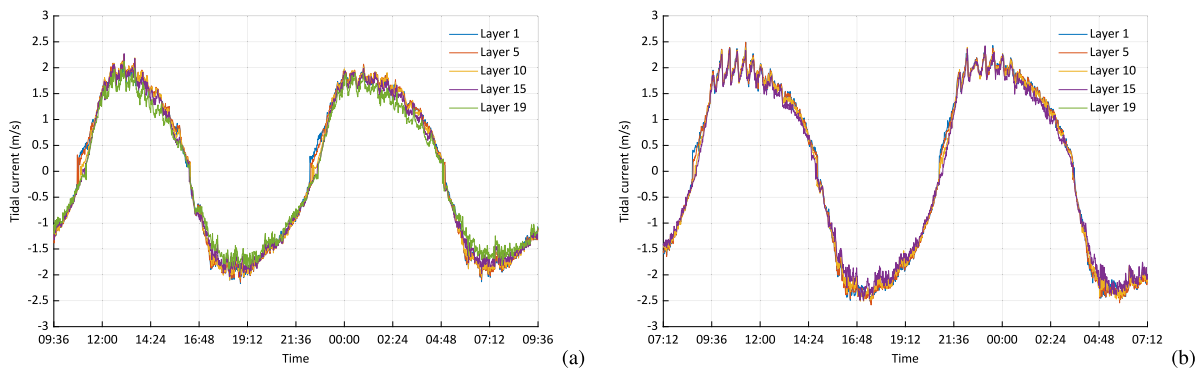


Fig. 6. Speed curves along the water column of the Boqueirão Channel. (a) Neap and (b) Spring tides.

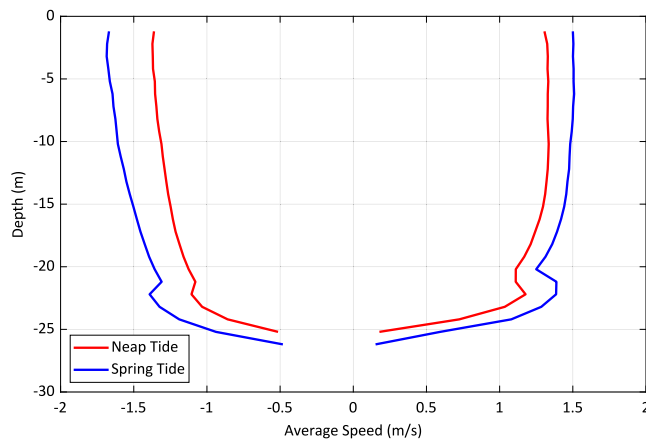


Fig. 7. Average speed of the measured velocities for each Channel depth during the neap and spring tides.

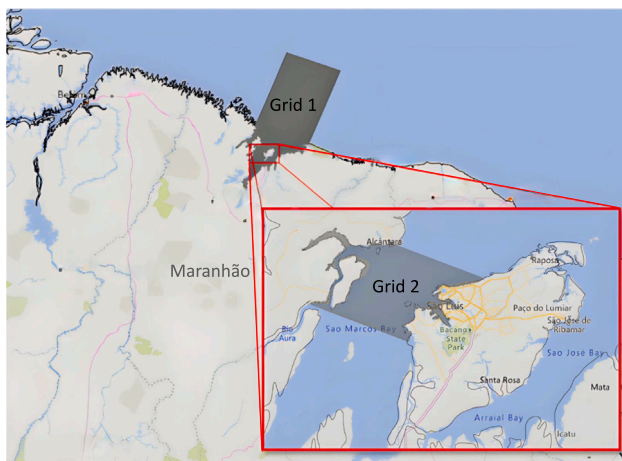


Fig. 8. Maps with a numeric domain location and grid nesting.

grids can follow the contours of the terrain and channels, avoiding stair-step-like boundaries [25].

Delft3D-FLOW uses parameters that can be configured on the basis of the features of the site that will be modeled. Some of these parameters are temperature, roughness, salinity and viscosity. The simulation requires the inclusion of external data, such as boundary conditions (level and sea currents) and data from the digital terrain model that represents the sea floor. These data were extracted from the TPXO (boundary conditions) and ETOPO (bathymetry) global models.

4.1. Three-dimensional numerical model

In this stage, the modeled area is defined in computational grids. Two grids were created. The first has lower resolution and a larger coverage area (called Grid 1, Fig. 8). The second grid is included in the first and has a higher resolution for the area of interest (Grid 2, Fig. 8). Grid 1 is less refined and includes the boundary conditions of the TPXO global model. Grid 2 includes the area between part of the coastal regions of the municipalities of Alcântara and São Luís. In this study, the ratio of resolutions between the two grids is 3:1 as recommended in [26]. This way, the resolution of grid 1 is 300 m, while the resolution of grid 2 is 100 m.

The data extracted from the global models determine the conditions for the model at the boundaries, which meant that Grid 1 covered a distance of approximately 150 km from the coast of the State of Maranhão, which includes a part of the continental slope.

Table 2
Tidal constituents

Constant	Period	Amplitude ^a	Description
Semidiurnal (hours)			
M2	12.42	100.00%	Principal lunar
S2	12	28.30%	Principal solar
N2	16.66	16.55%	Larger lunar elliptic
M4	6.21	2.30%	Overtides of principal lunar
K2	11.97	8.58%	Lunisolar
Diurnal (days)			
K1	0.99	5.53%	Lunar diurnal
O1	1.07	4.73%	Lunar diurnal
Q1	1.12	0.97%	Larger lunar elliptic
P1	1	1.62%	Solar diurnal
Long Period (days)			
MM	27.55	0.90%	Lunar monthly
MSF	14.76	1.03%	Lunisolar synodic fortnightly
MF	13.66	1.30%	Lunisolar fortnightly

^a Amplitude relative to M2 ($K = 1.95$).

Modeling the sea floor results in a numerical grid with the inclusion of the depth parameters [27]. Fig. 9.a and 9.b illustrate the depths of both grids respectively with The Boqueirão Channel (highlighted by the red rectangle). The maximum depth observed was 31 m, and due to the local morphology, the drainage flow carries a significant amount of energy towards the deepest point of the Channel, resulting in lower current velocities during ebb tide in the study area. This effect is not observed during flood tide, as in this situation, the local morphology does not present barriers, allowing a greater portion of the energy from the ocean to be directed towards the study area.

The data used to model Grid 2 were obtained by combining the following sources:

- Bathymetric data was collected in situ using a R2 Sonic 2022 Wideband multibeam echosounder, capable of operating at frequencies between 170 and 700 kHz [28]. For the processing phase, the Hysweep Editor 64-bit tool was used to assess the quality of the multibeam bathymetric survey;
- Nautical charts [19]; and
- ETOPO global model.

Taking the boundary conditions provided by TPXO as initial parameters, the model solves the Navier Stokes equations and the transport equations [25]. And finally, it results in the hydrodynamic flow pattern in the simulated domain.

It is important to note that the simulation was conducted with 10 layers of vertical stratification of the Channel's profile. Therefore, for the maximum depth of 31 m, each layer would have a thickness of 3.1 m. It was decided that, for the calculations of annual energy generation to be performed in the upcoming sections of this work, the velocity magnitudes from the surface layer (layer 1) of the simulation were used. The choice of using only one layer allows for a preliminary analysis of the turbine generation considered in this study, as seen in previous sections, where there were no significant variations in velocities along the vertical profile of the Boqueirão Channel. Fig. 10 shows the surface tidal current speeds obtained from the model for a spring tide on November 6, 2021 in São Marcos Bay, with speeds above 2.5 ms^{-1} .

The result of the simulation shows that this region is dominated by the main semidiurnal lunar component $M2$ with period of 12.42 h. The second most dominant component is the main solar $S2$, with a period of 12 h and an amplitude of 28.30% of the $M2$. As a result, the region has the typical features of a semi-diurnal tide. Table 2 lists all the components that have a value greater than 0.9% of the amplitude of $M2$.

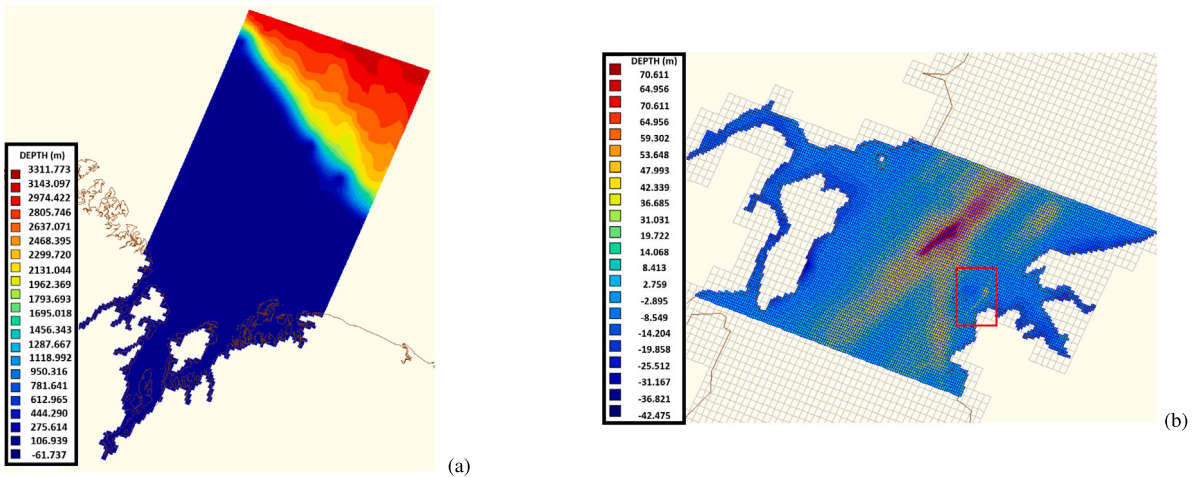


Fig. 9. 2D digital model in meters of Grid 1 floor (a); Grid 2 floor with the Boqueirão Channel highlighted by the red square (b).

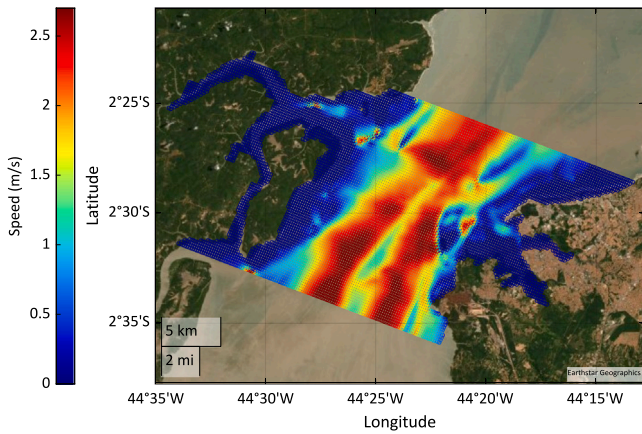


Fig. 10. Distribution of the tidal current speeds in São Marcos Bay.

Another interesting factor in the composition of the local tide, is the presence of bi-weekly components: synodic lunisolar MSF and MF , associated with full and new moons. Its influence can also be seen in the speed of the tidal currents. Fig. 11 shows the simulation results for tidal current magnitudes during the second lunar cycle of the year 2021. Higher velocities are observed during the phase of the full and new moons (spring tides) and lower velocities during the waxing and waning moon phases (neap tide).

4.2. Validation

The simulation's validation involved comparing it with current velocity magnitude data measured at the layer closest to the surface and at a depth of 16 m, within the same location and period. Fig. 12 illustrates the comparison between the magnitude of the measured surface velocity and the simulated surface velocity at the location closest to the real instrument location.

The comparison yielded notable results: for the surface, the coefficient of determination R^2 was 0.74, the mean square error was $0.06 \text{ m}^2\text{s}^{-2}$, and the coefficient of correlation was 0.86. At the depth of 16 m, the coefficient of determination R^2 was 0.6, the mean square error was $0.24 \text{ m}^2\text{s}^{-2}$, and the coefficient of correlation was 0.77. These findings suggest that the simulation exhibits a strong correlation with the measured data at the surface and a reasonably good correlation at the 16 m depth.

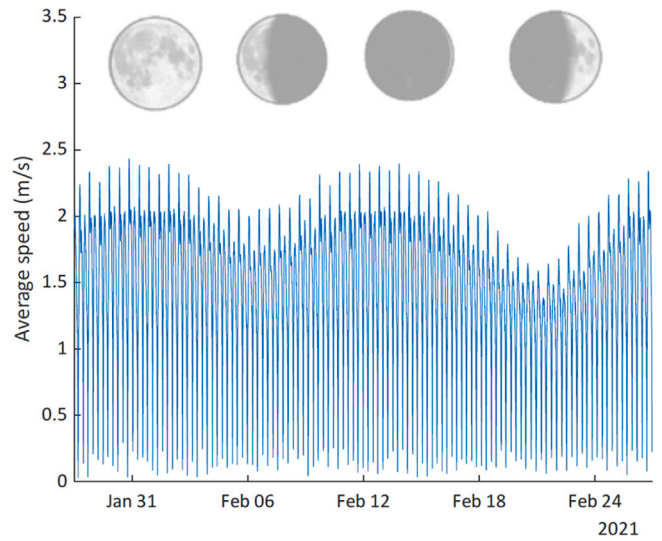


Fig. 11. Horizontal velocity amplitude during the second lunar cycle of 2021.

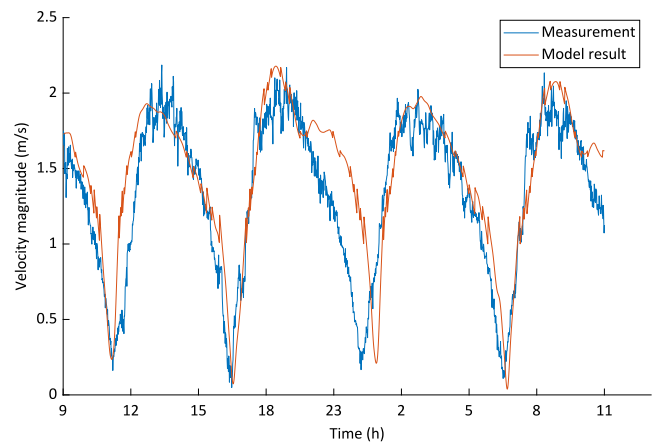


Fig. 12. Comparison between measured and simulated velocity magnitude.

5. Estimating the energy potential of the boqueirão channel

From the analysis of Fig. 7, it can be concluded that there is little variation in the vertical intensity of the current profile of the Channel.

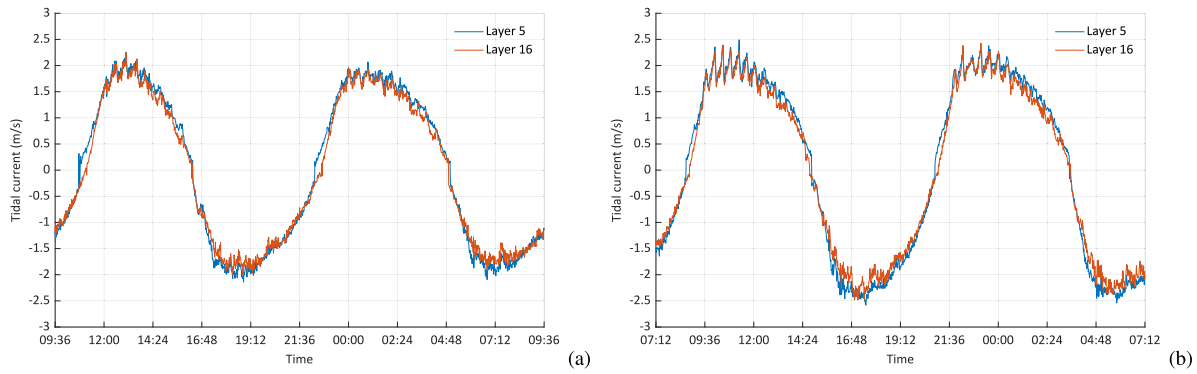


Fig. 13. Speed curves for depths of 5 and 16 meters in the Boqueirão Channel (a) For data obtained from the neap tide; and (b) For data from the spring tide.

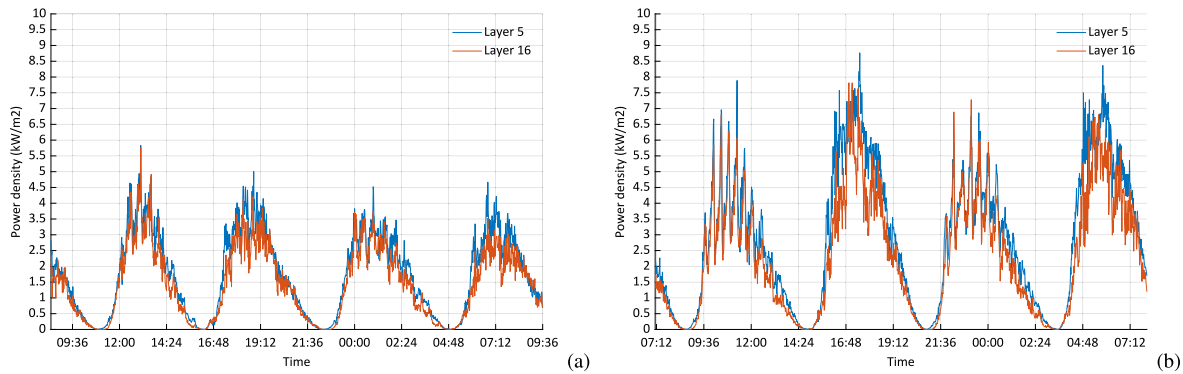


Fig. 14. Power density curves for 5 and 16 m depth for neap tide (a); and spring tide (b).

For example, between the surface and the depth of 16 m, there was a variation of 0.13 and 0.19 ms⁻¹ in the flood of campaigns 1 and 2. For the ebb, the variation was 0.07 and 0.09 ms⁻¹.

Still regarding the depth of up to 16 m, the average of the velocities obtained during the floods was calculated, and ebbs of the two campaigns. For the neap tide campaign, the mean velocities were 1.33 and 1.3 ms⁻¹ for flood and ebb periods, respectively. In the spring tide, the average velocities in the flood and ebb periods were of 1.62 and 1.48 ms⁻¹, respectively. Thus, depths of up to 16 m are attractive for tidal exploration, since the bottom edge effect is reduced.

Figs. 13.a and 13.b illustrate the current velocity magnitude graphs for depths of 5 and 16 m, for neap and spring tide respectively.

Velocity data from the bounded area of the vertical profile to a depth of 16 m, are used to estimate the power density, as expressed in the following equation

$$D_p = \frac{1}{2} \rho v^3 \tag{1}$$

Where:

D_p is the power density (kWm⁻²);

ρ is the average water density in the Boqueirão Channel measured using CTD data in the neap tide period (1019.66 kgm⁻³);

v is the speed of the water (ms⁻¹) [29].

Figs. 14.a and 14.b illustrate the power density for each minute of the measurement campaign at neap and spring tides, respectively. The highest power density found in the neap mooring period was 6.32 kWm⁻² at a depth of 13 m, while the highest value found for the spring mooring was 8.77 kWm⁻² at a depth of 5 m.

Fig. 15 shows the average power densities throughout the periods of the neap tide and spring tide campaigns for depths of up to 16 m, including periods of low tide.

Figs. 16.a and 16.b illustrate the average cumulative power densities, calculated as the mean of the average power densities for each meter in the vertical profile up to 16 m for spring and neap tides,

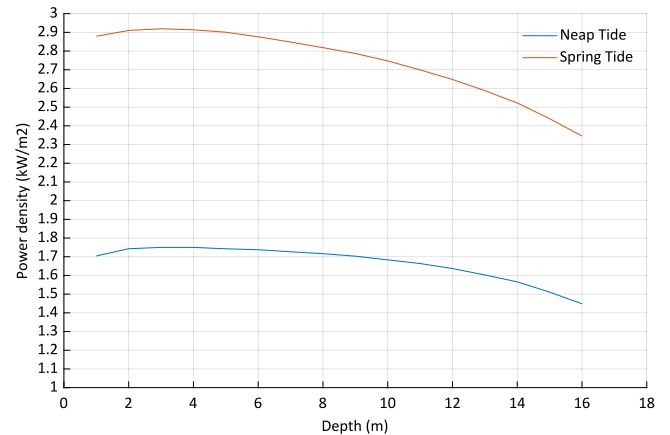


Fig. 15. Power density through the vertical profile.

respectively. The mean power density considering all depth levels evaluated, both for spring and neap tides, were 2.74 kWm⁻² and 1.66 kWm⁻², respectively.

To determine the accumulated power densities both in the flood and in the ebb of the two campaigns, the power density was calculated at each velocity measured for depths of up to 16 m (recalling that negative velocities refer to the flood tide and the positive to the ebb tide). Then, the power density values for each velocity measured in the campaigns were added, both for flood and ebb. It is observed that the power densities in the flood were clearly higher than in the ebb. During the neap tide, the power density for the flood and ebb was 21 MWm⁻² and 19.21 MWm⁻², respectively. During spring tide, the difference between flood and ebb was more notable: 37.17 MWm⁻² for flood and 28.41 MWm⁻² for ebb.

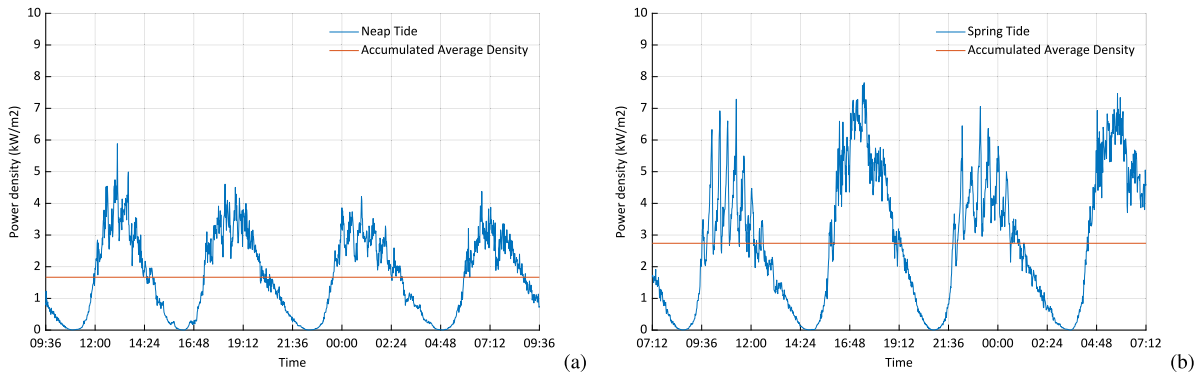


Fig. 16. Accumulated power density of the vertical profile of the Boqueirão Channel (a) Campaign 1 and (b) Campaign 2.

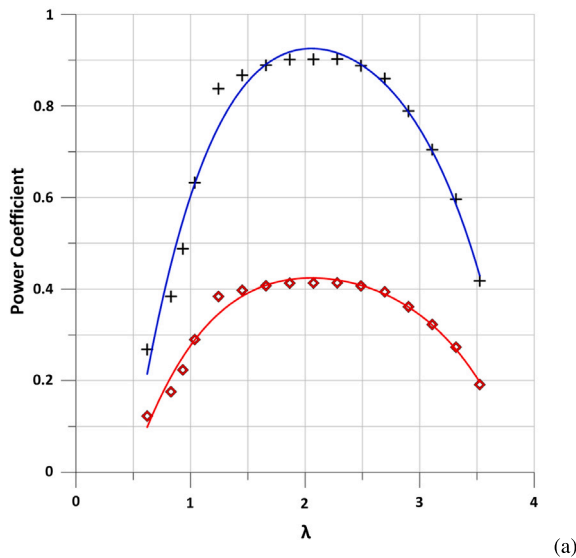


Fig. 17. (a) HDAT Performance and (b) prototype.

This difference in power density between the ebb and flood can be attributed to the geometrical shape of the estuary that includes asymmetries which lead to a non-linear pattern.

5.1. Hydrokinetic turbine

The theoretical Betz limit states that the maximum power extractable by a turbine in a free flow is approximately 59% of the power available in the flow without the turbine [11]. One way to get around the problem of this efficiency constraint is to use HDATs [12]. In this article, the turbine designed in [30] is considered. To obtain the turbine performance, it was numerically modeled in ANSYS Fluent [31] under conditions of free flow velocity fixed at 2.4 ms^{-1} , while the rotor angular velocity was altered to create different speed ratio conditions at the tip of the blade. Fig. 17.a shows that the turbine reaches its maximum level of performance with a power coefficient normalized by the diameter of the throat (C_p) equal to 0.905 and by the external area of the diffuser (C_p^*) equal to 0.415 for a tip-speed-ratio value (λ) equal to 2.13.

Fig. 17.b illustrates the prototype of the project with a rotor diameter of 1 m. Its dimensions can be scaled up to an external diffuser diameter of 6 m, based on geometric similarity of turbomachinery theory [32].

Fig. 18 illustrates that the output power does not increase proportionally with the increase in turbine diameter. This is due to the power coefficient that has a non-linear behavior and with optimal values that depend on the geometry and speed of the flow [33].

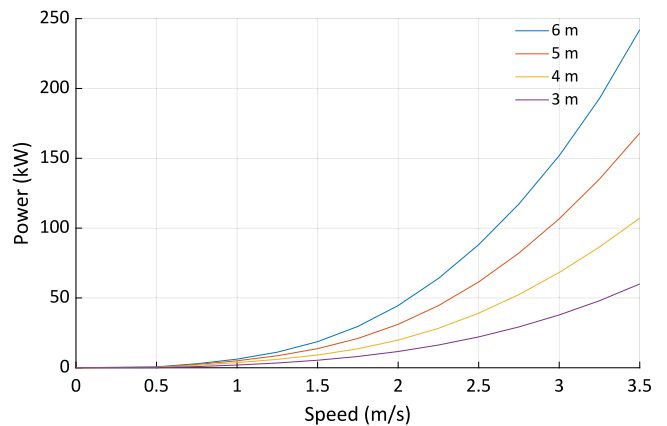


Fig. 18. Turbine power curve for diffuser external areas of different dimensions.

A usual motivation for carrying out a renewable energy project is the desire to obtain the maximum possible extractable energy from a given site. However, there are different kinds of restrictions that prevent this from being fully possible. These include the following:

- Channel Depth;
- Available area;

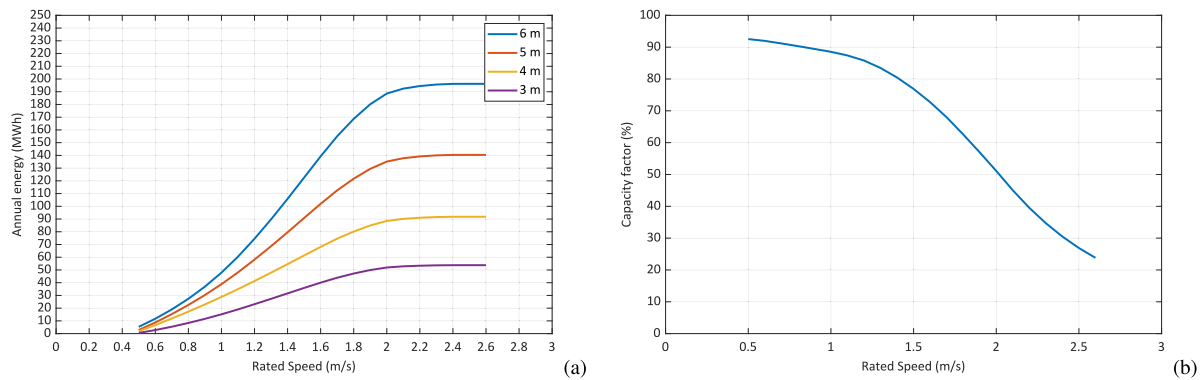


Fig. 19. (a) Annual energy vs rated speed; (b) Capacity factor vs rated speed for turbines with diffuser diameters of 6, 5, 4 and 3 m.

Table 3

Summary of HDAT specifications Source: [30].

HDAT				
$D_{External}$ (m)	6	5	4	3
D_{Throat} (m)	3.98	3.32	2.65	1.99
V_{Cut-in} (ms^{-1})	approx 0.5	approx 0.5	approx 0.5	approx 0.5
V_R (ms^{-1})	2	2	2	2
Rated Power(P_R) (kW)	45	31	20	12
A (m^2)	12.45	8.65	5.53	3.11

- Tidal current speed;
- Size of the turbine (a reasonable size is necessary in the techno-economic relationship);
- Annual power generation (GWh) ratio v-s technical feasibility.

The Boqueirão Channel has depths of up to 31 m, that restricts the diameter of the turbine that will be used in a hydrokinetic plant. As can be seen in Fig. 7, the velocity gradient near the Channel surface is smaller. The higher shear in the region closest to the bed would lead to a poor turbine performance. Thus, a feasible depth in the Channel is around 16 m.

The curve in Fig. 19.a represents the yearly energy for each rated speed while 19.b, illustrates the capacity factor (CF) vs rated speed. Both graphs were plotted for 4 HDAT diameters.

For instance, considering the speeds obtained from the simulation illustrated in the previous sections, the turbine cut-out speed of $2 ms^{-1}$ and cut-in of $0.5 ms^{-1}$, the CF will be equal to 51% and the yearly generations will be equal to 188.56, 135.13, 88.49 and 51.93 MWh for the diameters of 6, 5, 4 and 3 m, respectively. If $1.5 ms^{-1}$ is considered, the CF increases to 77%. However, there would be a considerable reduction in the annual energy: 34, 29, 27 and 28%, respectively in comparison with the previous case. In the case of $2.5 ms^{-1}$ there will be a significant reduction in the CF which will remain at around 26% with little increase in the total annual amount of energy produced by each HDAT. From this analysis and in light of Table 1, an appropriate turbine for this site should have a cut-in speed of $0.5 ms^{-1}$ and a rated speed of about $2 ms^{-1}$.

In this work, the estimated cost for turbines with 6, 5, 4 and 3 m in diameter is analyzed. Note that in the final choice of the turbine, other factors must be taken into account, such as the availability of mature local technology, logistical costs, as well as the degree of risk that investors would be willing to face. The output powers for each turbine diameter are estimated from the curves in Fig. 18. Note that in this figure, the output power does not increase proportionally with the increase in turbine diameter. This is due to the power coefficient that has a non-linear behavior and with optimal values that depend on the geometry and speed of the flow. Table 3 shows the specifications of the turbines.

6. Hydrokinetic farm designing

After characterizing the site and selecting the HDATs, we can proceed to design the hydrokinetic farm that would be supported by the area, in light of the restrictions outlined above. When making hydrokinetic arrangements, it is important to define the spacing between the turbines so that the wake generated by the upstream turbine does not disturb the flow at the entrance of the downstream turbine. This is because it would result in a reduction in the efficiency of the latter. In addition, wake can cause mechanical stresses to the structure, as well as in the mechanical anchoring system [34].

The behavior of wake turbulence is quite complex. A distinction can be made between nearby wakes and distant wakes. The nearby wakes is characterized by a drop in velocity and increase in turbulent flow generated by the abrupt drop in pressure downstream of the turbine. In the distant wakes, there is a speedy recovery and a turbulence intensity reduction [35]. Fig. 20 shows the turbulent velocity profiles at different positions downstream of rotor, where in the most distant position, the velocity profile becomes uniform again, owing to the dissipation of the turbulent energy.

In [36] it was concluded that the larger the diameter of the turbine, the greater the volume of flow that passes through it and hence an increase in the resulting turbulent flow. However, there is no convergence of opinion among current researchers about what analytical expression or single criterion should be employed to define the distance between the turbines. Table 4 lists several research studies within the scientific literature, that use experimental methods and/or computer simulations to calculate the length of the wakes as a function of the diameter (D) of the turbine (see Table 4).

In this article, the worst case scenario was adopted, i.e. the greatest longitudinal distance ($40D$) and the greatest lateral distance ($2.5D$) from within the bibliographical survey of Table 4. As a result, the longitudinal distance for the turbines will be 160 m longitudinally and 10 m laterally.

Fig. 21 highlights both the ferry boat and São Luís - Alcântara navigation routes, by means of blue dashed lines. Given the fact that a safe distance is at least 500 m from these routes, the feasible region has an approximate length of 3000 m. To avoid the edge effect and shallow areas, it was decided to keep a distance of approximately 200 m from both coastal edges. Thus there is a potential area available of around $500 m \times 3000 m$. In Fig. 21 the suggested region is highlighted in red.

For the width of the proposed area, a lateral composition of 67, 51, 41 and 34 HDATs with diameters of 3, 4, 5 and 6 m, respectively, is possible. As previously calculated, each respective turbine generates 51.93, 88.49, 135.13 and 188.56 MWh annually taking into account the cut-in speed of $0.5 ms^{-1}$ and cut-out speed of $2 ms^{-1}$ for the turbines. The speeds are simulated for the whole year as explained in the previous sections. Hence, it would be possible to install a row of HDATs with diameters of 3, 4, 5 and 6 m respectively, which could

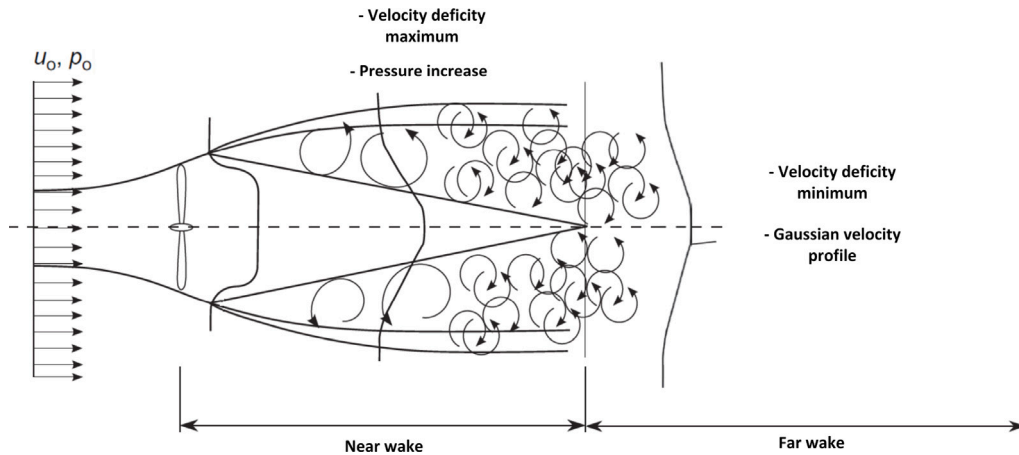


Fig. 20. Illustration of wake turbulence.
Source: [35].

Table 4
Study of wake length generated by turbulence in hydrokinetic turbines.

Wake length	Turbine diameter (m)	Ref.	Year
10 D lengthwise to recover 80% of its initial velocity	0.8	[37]	2009
16.5 D lengthwise to recover 75% of its initial velocity	10	[38]	2014
2.5 D laterally and 6 D lengthwise	0.53	[39]	2016
12 D lengthwise to regain 100% of its initial velocity	10	[35]	2016
20 D lengthwise to recover 85% of its initial velocity	0.28	[40]	2018
40 D lengthwise	1.5	[41]	2019
10 D à 12 D lengthwise to recover the initial velocity	0.27	[34]	2019
10 D lengthwise to recover 85% of its initial velocity	0.5	[42]	2020
7.3 D lengthwise	4	[43]	2021

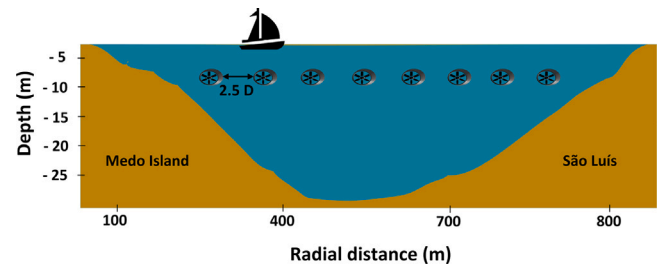


Fig. 22. Rough sketch of the position of the HDAT.

with diameters of 3, 4, 5 and 6 m, respectively. The total energy would thus be 90.46, 85.75, 88.65 and 83.34 GWh. These values refer to a very optimistic performance as they ignore the shadow effect between the rows of turbines.

As stated in previous sections, the depth levels up to 16 m have the highest average speeds and a homogeneous profile. Fig. 22 provide a rough sketch of the positioning of a row of HDATs, anchored in a floating system. Each can be installed at a depth of approximately 10 m, spaced at 2.5D. The distance from the edges of both islands is at least 200 m.

7. Estimated costs

As the HDAT projects are still in an early stage of development, the data to estimate the costs of these projects [44] are limited. However, We can estimate costs using similar tidal designs adapted to this case, by approximating the components that form a part of the Levelized Cost of Energy (LCOE). The LCOE expression used here is as follows:

$$LCOE = \frac{CAPEX + \sum_{t=1}^n \frac{OPEX_t}{(1+r)^t}}{\sum_{t=1}^n \frac{\text{Annual Energy Production}_t}{(1+r)^t}} \quad (2)$$

Where:

- LCOE: Levelised Cost of Energy (\$/kWh);
- CAPEX: Capital expenditure;
- OPEX_t: Operational expenditure (at year t);
- r: Discount rate;
- n: Lifetime of the system;
- t: Year from start of project [45].

In this article, we assume that capital costs occur in Year 0, the farm operation starts in Year 1 and has a lifetime of 25 years.



Fig. 21. Site for installation of the hydrokinetic farm.

generate around 3.48, 4.51, 5.54 and 6.41 GWh annually. With regard to the total area available for installing the hydrokinetic farm (1.5 km²), in theory, it would be possible to install 1742, 969, 656 and 442 HDATs

Table 5
HDAT estimated cost and CAPEX.

HDAT				
$D_{External}$ (m)	6	5	4	3
Estimated Cost (2020)	\$86,801.96	\$65,391.74	\$46,867.39	\$31,788.19
Estimated Cost (2021)	\$92,878.09,	\$69,969.16	\$50,148.10	\$34,013.36
CAPEX (2021)	\$232,195.23,	\$174,922.90	\$125,370.28	\$85,033.40

Table 6
HDAT OPEX.

HDAT				
$D_{External}$ (m)	6	5	4	3
Annual OPEX per Turbine	\$10,448.79	\$7,871.53	\$5,641.66	\$3,826.50
Annual OPEX per Row of Turbines	\$355,258.69	\$322,732.75	\$287,724.78	\$256,375.70

Table 7
HDAT annual generation and LCOE:.

HDAT				
$D_{External}$ (m)	6	5	4	3
Annual Generation per Turbine (MWh)	188.57	135.14	88.49	51.93
LCOE (\$kWh ⁻¹)	0.161	0.169	0.185	0.214

7.1. CAPEX

In [46], a similar but smaller HDAT developed by Smart Hydro Germany was used. The reported cost was \$16,342.00, which included components such as generator, mechanical protection shield, anchor, electrical cables, electrical panel, inverter and controller. The rated power was 5 kW (2.8 ms⁻¹) for a diameter of approximately 3 m and a weight of 380 kg. By using the Rule of Six Tenths (3), we can extrapolate this cost and get an approximation of the cost of our HDAT, as follows [47–49]:

$$\frac{Cost_A}{Cost_B} = \left(\frac{Cap_A}{Cap_B} \right)^M \quad (3)$$

Where:

M is the measurement of the economy of scale usually employed in the industrial sector;

$Cost_A$ and $Cost_B$ are the costs of turbines A and B ;

Cap_A and Cap_B are the rated power of turbines A and B .

The value of M for a hydrokinetic plant can be approximated to 0.76 [50]. From the Smart Hydro Germany turbine values (A), and considering the turbines rated power of Table 3 (B), the estimated cost will be around \$86,801.96, \$65,391.74, \$46,867.39 and \$31,788.19, for turbines with diameter of 6, 5, 4 and 3 m, respectively.

When the cost of this turbine is updated through the 2021 PCE (7%) [51] it rises to \$92,878.09, \$69,969.16, \$50,148.10 and \$34,013.36. According to [52], the cost of the turbine acquisition corresponds to 41% of CAPEX, 26% for foundation costs, 15% installation costs, 13% cabling costs and 5% costs for connection to the grid. In another project [53] the reported cost for the turbine is equivalent to 39% of the CAPEX value. Thus, it is reasonable to assume that the cost of HDAT corresponds to 40% of the project's CAPEX. Which leads us to a CAPEX estimate of \$232,195.23, \$174,922.90, \$125,370.28 and \$85,033.40. Table 5 shows the costs calculated for the year 2020, those estimated for 2021 and the CAPEX for each turbine, respectively.

7.2. Operation & maintenance costs

In [54], the O&M costs are estimated, both for scheduled and unscheduled maintenance, and take account of discrete 5-year intervals over the 25-year lifetime of the project. Taking the average of these values, an annual cost for O&M of 4.5% of the HDAT CAPEX is obtained. In [55] the annual O&M cost of approximately 3.42% of CAPEX is taken as a reference-point, while in [56], the ratio between

CAPEX and annual OPEX was approximately 1.52%. Thus, the value of 4.5% of CAPEX can be adopted as a “pessimistic” scenario. In light of these criteria, the annual OPEX cost per turbine and for each turbine row is shown in the Table 6.

7.3. Levelized cost of energy - LCOE

Let us consider a lifetime of 25 years and a discount rate (r) of 7 % per year [51]. Substituting the annual generation values of each turbine in Eq. (2), the LCOE is calculated, as shown in Table 7.

This results is close to the range estimated by IRENA [2], where the LCOE for tidal energy is between 0.20–0.45 \$kWh⁻¹. The better LCOE achieved here can be largely attributed to the gain in turbine performance caused by the augmented-diffuser design.

8. Conclusion

This article presented the modeling and energetic characterization of tidal energy in the Boqueirão Channel. According to the measurement campaigns carried out in spring and neap tide periods, the mean power densities of the Channel were 2.74 kWm⁻² and 1.66 kWm⁻², respectively. Then, as a case study and taking into account the restrictions of the estuary, a hydrokinetic farm is designed considering HDAT with optimized topology, taking into account the wake effect. The main contributions of this article are:

- Hydrodynamic modeling of the site using measured data;
- Show the energy tidal viability of the estuary;
- To reinforce, through this case study, the importance of sites with intermediate tidal currents.
- To illustrate the feasibility of using HDATs in a tidal stream farm.

From on-site measurements, the model was properly calibrated, allowing to show good power and energy density. The Boqueirão Channel is located in São Marcos Bay, but it has no restrictions due to its use in commercial navigation. The depth in its usable span is in the order of 16 m, with a width of 500 m. the shear of currents to different depths is minimal, being an attractive feature for energy projects. Despite the good energy density, the speed of currents rarely exceeds 2 ms⁻¹. Therefore, to improve performance, the use of HDAT was suggested. The simulations show that this alternative brings efficiency gains to the park, indicating an interesting LCOE value ranging from 0.161 to 0.214 \$kWh⁻¹ considering the analyzed turbine diameters. The authors acknowledge that one aspect that needs further research is the wake effect. In this work, more rigorous distancing criteria were assumed, in order to have more realistic results, which provide a reliable basis for the various possible projects in the north coast of Brazil and in the Amazon region.

Declaration of competing interest

The authors declare that they have no known competing financial interests or personal relationships that could have appeared to influence the work reported in this paper.

References

- [1] BP Energy, Statistical review of world energy 2021, BP Energy Outlook 2021 (70) (2021).
- [2] IRENA, Innovation outlook: Ocean energy technologies, 2020.
- [3] O. Edenhofer, R. Pichs-Madruga, Y. Sokona, K. Seyboth, P. Matschoss, S. Kadner, T. Zwickel, P. Eickemeier, G. Hansen, S. Schlömer, et al., IPCC special report on renewable energy sources and climate change mitigation, 2011, Prepared By Working Group III of the Intergovernmental Panel on Climate Change, Cambridge University Press, Cambridge, UK.
- [4] J.-H. Chen, X.-C. Wang, H. Li, C.-H. Jiang, L.-J. Bao, Design of the blade under low flow velocity for horizontal axis tidal current turbine, *J. Mar. Sci. Eng.* 8 (12) (2020) [Online]. Available: <https://www.mdpi.com/2077-1312/8/12/989>.
- [5] D. Fouz, R. Carballo, I. López, G. Iglesias, Tidal stream energy potential in the Shannon estuary, *Renew. Energy* 185 (C) (2022) 61–74, [Online]. Available: <https://ideas.repec.org/a/eee/renene/v185y2022icp61-74.html>.
- [6] Z. Yang, T. Wang, R. Branch, Z. Xiao, M. Deb, Tidal stream energy resource characterization in the Salish Sea, *Renew. Energy* 172 (2021) 188–208, [Online]. Available: <https://www.sciencedirect.com/science/article/pii/S0960148121003827>.
- [7] J.I. Encarnacion, C. Johnstone, S. Ordonez-Sanchez, Design of a horizontal axis tidal turbine for less energetic current velocity profiles, *J. Mar. Sci. Eng.* 7 (7) (2019) [Online]. Available: <https://www.mdpi.com/2077-1312/7/7/197>.
- [8] T.L.C. Gomes, O.R. Saavedra, P.L. Bezerra, B.G. Sá, R.A. Soares, Scenario analysis for sizing of micro-plants of tidal currents for isolated systems, in: 2019 IEEE PES Innovative Smart Grid Technologies Conference - Latin America, ISGT Latin America, 2019, pp. 1–6.
- [9] W. Tian, Z. Mao, H. Ding, Design, test and numerical simulation of a low-speed horizontal axis hydrokinetic turbine, *Int. J. Naval Archit. Ocean Eng.* 10 (6) (2018) 782–793, [Online]. Available: <https://www.sciencedirect.com/science/article/pii/S2092678217301978>.
- [10] V. Ramos, R. Carballo, M. Álvarez, M. Sánchez, G. Iglesias, A port towards energy self-sufficiency using tidal stream power, *Energy* 71 (2014) 432–444, [Online]. Available: <https://www.sciencedirect.com/science/article/pii/S0360544214005295>.
- [11] A. Betz, Theoretical limit for best utilization of wind by wind-motors, *Mag. Entire Turb. Syst.* 20 (1920) 307–309.
- [12] M. Barbarić, Z. Guzović, Investigation of the possibilities to improve hydrodynamic performances of micro-hydrokinetic turbines, *Energies* 13 (17) (2020) [Online]. Available: <https://www.mdpi.com/1996-1073/13/17/4560>.
- [13] C. Mastaller, J. Wack, S. Riedelbauch, Investigation of the operating principle of diffuser augmented hydrokinetic turbines, *IOP Conf. Ser.: Earth Environ. Sci.* 774 (2021) 012138.
- [14] P.A. Silva, T.F. Oliveira, A.C. Brasil Junior, J.R. Vaz, Numerical study of wake characteristics in a horizontal-axis hydrokinetic turbine, *Anais da Acad. Bras. de Ciências* 88 (2016) 2441–2456.
- [15] E. González-Gorbeña, P. Rosman, R. Qassim, Assessment of the tidal current energy resource in São Marcos Bay, Brazil, *J. Ocean Eng. Mar. Energy* 1 (2015).
- [16] A. Czizewski, F.M. Pimenta, O.R. Saavedra, Numerical modeling of Maranhão Gulf tidal circulation and power density distribution, *Ocean Dyn.* 70 (5) (2020) 667–682.
- [17] R.B. de Sousa Veras, A.M.S. Costa, D.L.S. Cosme, O.R. Saavedra, A.C. Czizewski, A.R.T. Junior, F.M. Pimenta, Modeling tidal streams of the boqueirão channel using Delft3D, in: TENCON 2021-2021 IEEE Region 10 Conference, TENCON, IEEE, 2021, pp. 911–916.
- [18] E. Castro, A. Moraes, E. Pinheiro, J. Pontes, Zoneamento geomorfológico da ilha do medo-ma., *Rev. Geonorte* 5 (15) (2014) 150–155.
- [19] Marinha, Dados maregráficos e fluviométricos, 2022, [Online]. Available: <https://www.marinha.mil.br/chm/dados-do-segnav/dados-de-mare-mapa>.
- [20] S.R. Dillenburg, P.A. Hesp, Geology and Geomorphology of Holocene Coastal Barriers of Brazil, Vol. 107, Springer Science & Business Media, 2008.
- [21] L.D. de Lacerda, A.C. Ferreira, R. Borges, R. Ward, Mangroves of Brazil, in: S.C. Das, Pullaiah, E.C. Ashton (Eds.), *Mangroves: Biodiversity, Livelihoods and Conservation*, Springer Nature Singapore, Singapore, 2022, pp. 521–563, http://dx.doi.org/10.1007/978-981-19-0519-3_20.
- [22] L.C.B. Molion, S.O. Bernardo, Uma revisão da dinâmica das chuvas no nordeste brasileiro, *Rev. Bras. de Meteorol.* 17 (1) (2002) 1–10.
- [23] INMET, National institute of meteorology, 2022, [Online]. Available: <https://portal.inmet.gov.br/paginas/luas>.
- [24] E. González-Gorbeña, P.C. Rosman, R.Y. Qassim, Assessment of the tidal current energy resource in São Marcos Bay, Brazil, *J. Ocean Eng. Mar. Energy* 1 (4) (2015) 421–433.
- [25] D. Deltares, Delft3D-FLOW user manual, 2013, Deltares Delft, the Netherlands, Vol. 330.
- [26] B. Boersma, M. Kooper, T. Nieuwstadt, P. Wesseling, Local grid refinement in large-eddy simulation, *J. Eng. Math.* 32 (2) (1997) 161–175.
- [27] D. Deltares, Delft3D-FLOW simulation of multi-dimensional hydrodynamic flows and transport phenomena, including sediments, 2013, Delft Hydraulics, Delft.
- [28] R2SONIC, Sonic 2022 and integrated sonic 2022 - wideband multibeam echosounder range, 2022, [Online]. Available: https://www.r2sonic.com/wp-content/uploads/2023/05/2022-V_US-online-04.2023-1.pdf.
- [29] S.P. Neill, M.R. Hashemi, *Fundamentals of Ocean Renewable Energy: Generating Electricity from the Sea*, Academic Press, 2018.
- [30] T.J. Rezek, R.G.R. Camacho, N. Manzanares-Filho, A novel methodology for the design of diffuser-augmented hydrokinetic rotors, *SSRN* (2022) 1–34.
- [31] ANSYS, Inc. ANSYS FLUENT theory guide, 2015, USA.
- [32] R.S.R. Gorla, A.A. Khan, *Turbomachinery Design and Theory*, Marcel Dekker, Inc., 2003.
- [33] C. Niebuhr, M. van Dijk, V. Neary, J. Bhagwan, A review of hydrokinetic turbines and enhancement techniques for canal installations: Technology, applicability and potential, *Renew. Sustain. Energy Rev.* 113 (2019) 109240, [Online]. Available: <https://www.sciencedirect.com/science/article/pii/S136403211930440X>.
- [34] P. Ouro, L. Ramírez, M. Harrold, Analysis of array spacing on tidal stream turbine farm performance using Large-Eddy simulation, *J. Fluids Struct.* 91 (2019) 102732.
- [35] P. Strobel, T. Oliveira, A. Brasil Junior, J. Vaz, Numerical study of wake characteristics in a horizontal-axis hydrokinetic turbine, *Anais da Acad. Bras. de Ciências* 88 (2016).
- [36] V.G. Nago, I.F.S. dos Santos, M.J. Gbedjinou, J.H.R. Mensah, G.L. Tiago Filho, R.G.R. Camacho, R.M. Barros, A literature review on wake dissipation length of hydrokinetic turbines as a guide for turbine array configuration, *Ocean Eng.* 259 (2022) 111863, [Online]. Available: <https://www.sciencedirect.com/science/article/pii/S0029801822012069>.
- [37] L. Myers, A. Bahaj, Near wake properties of horizontal axis marine current turbines, in: *Proceedings of the 8th European Wave and Tidal Energy Conference*, 2009.
- [38] M. Edmunds, R. Malki, A. Williams, I. Masters, T. Croft, Aspects of tidal stream turbine modelling in the natural environment using a coupled BEM-CFD model, *Int. J. Mar. Energy* 7 (2014) 20–42, [Online]. Available: <https://www.sciencedirect.com/science/article/pii/S2214166914000186>.
- [39] J. Riglin, C. Daskiran, J. Jonas, W.C. Schleicher, A. Oztekin, Hydrokinetic turbine array characteristics for river applications and spatially restricted flows, *Renew. Energy* 97 (2016) 274–283, [Online]. Available: <https://www.sciencedirect.com/science/article/pii/S0960148116304918>.
- [40] M. Nuernberg, L. Tao, Experimental study of wake characteristics in tidal turbine arrays, *Renew. Energy* 127 (2018) 168–181, [Online]. Available: <https://www.sciencedirect.com/science/article/pii/S0960148118304610>.
- [41] M. Guerra, J. Thomson, Wake measurements from a hydrokinetic river turbine, *Renew. Energy* 139 (2019) 483–495, [Online]. Available: <https://www.sciencedirect.com/science/article/pii/S096014811930206X>.
- [42] C. Hill, V.S. Neary, M. Guala, F. Sotiropoulos, Performance and wake characterization of a model hydrokinetic turbine: The reference model 1 (RMI) dual rotor tidal energy converter, *Energies* 13 (19) (2020) [Online]. Available: <https://www.mdpi.com/1996-1073/13/19/5145>.
- [43] I.F.S. dos Santos, R.G.R. Camacho, G.L. Tiago Filho, Study of the wake characteristics and turbines configuration of a hydrokinetic farm in an Amazonian river using experimental data and CFD tools, *J. Clean. Prod.* 299 (2021) 126881.
- [44] R.D. Montoya Ramírez, F.I. Cuervo, C.A. Monsalve Rico, Technical and financial valuation of hydrokinetic power in the discharge channels of large hydropower plants in Colombia: A case study, *Renew. Energy* 99 (2016) 136–147, [Online]. Available: <https://www.sciencedirect.com/science/article/pii/S0960148116305717>.
- [45] J. Chozas, International levelised cost of energy for ocean energy technologies, *Ocean Energy Syst.* (2015).
- [46] B. Kirke, Hydrokinetic turbines for moderate sized rivers, *Energy Sustain. Dev.* 58 (2020) 182–195, [Online]. Available: <https://www.sciencedirect.com/science/article/pii/S0973082620302842>.
- [47] C.H. Chilton, Six-tenths factor applies to complete plant costs, *Chem. Eng.* (1950).
- [48] R. Williams Jr., Six-Tenths Factor Aids in Approximating Costs, *Chem. Eng.* 54 (1947) 124–125.
- [49] P. Berthouex, Evaluating economy of scale, *Water Pollut. Control Fed.* 44 (11) (1972) 2111–2119, [Online]. Available: <https://www.jstor.org/stable/25037656>.
- [50] D. Garrett, *Chemical Engineering Economics*, reprint, Springer, 1989, 2013.
- [51] Graphics for economic news releases, 2022, [Online]. Available: <https://www.bls.gov/charts/consumer-price-index/consumer-price-index-by-category-line-chart.htm>.
- [52] A. Vazquez, G. Iglesias, Capital costs in tidal stream energy projects – A spatial approach, *Energy* 107 (2016) 215–226, [Online]. Available: <https://ideas.repec.org/a/eee/energy/v107y2016icp215-226.html>.
- [53] Department for Business Energy & Industrial Strategy, Lessons learnt from MeyGen phase 1A final summary report, 2020, [Online]. Available: <https://webassets.bv.com/2020-06/MeyGen%20Lessons%20Learn%20Full%20Report.pdf>.

- [54] M. Tigabu, Economics of hydro-kinetic turbine for off-grid application: A case study of Gumara River, Upper Blue Nile, Amhara, Ethiopia, *Int. J. Renew. Energy Res.* 9 (2019) 1368–1375.
- [55] T. Xia, M. Rezaei, U. Dampage, S.A. Alharbi, O. Nasif, P.F. Borowski, M.A. Mohamed, Techno-economic assessment of a grid-independent hybrid power plant for co-supplying a remote micro-community with electricity and hydrogen, *Processes* 9 (8) (2021) [Online]. Available: <https://www.mdpi.com/2227-9717/9/8/1375>.
- [56] T.T. Tran, A.D. Smith, Incorporating performance-based global sensitivity and uncertainty analysis into LCOE calculations for emerging renewable energy technologies, *Appl. Energy* 216 (2018) 157–171, [Online]. Available: <https://www.sciencedirect.com/science/article/pii/S0306261918301430>.